Crustal Imaging with Noisy Teleseismic Receiver Functions Using Sparse Radon Transform

Ziqi Zhang[1,2,3] and Tolulope Olugboji[4]

[1]Department of Earth and Environmental Sciences, University of Rochester
[2]Department of Electrical and Computer Engineering, University of Rochester
[3]Georgen Institute of Data Sciences, University of Rochester
[4]Affiliation not available

November 8, 2023

Crustal Imaging with Noisy Teleseismic Receiver Functions Using Sparse Radon Transform

Ziqi Zhang[1]

Tolulope Olugboji[123]

[1]Department of Earth and Environmental Sciences, University of Rochester, Rochester, NY 14627, USA
[2]Department of Electrical and Computer Engineering, University of Rochester, Rochester, NY 14627, USA
[3]Georgen Institute of Data Sciences, University of Rochester, Rochester, NY 14627, USA

Key Points:

- Sparse Radon transform is used to de-noise the Ps-RF and extract Moho-related phases.
- Synthetic and data examples show that our approach can drastically reduce the ambiguity of $H-\kappa$ stacking.
- Our approach can be coupled with resonance filtering to improve crustal imaging in reverberant settings.

Declaration of Competing Interests:

The authors acknowledge there are no conflicts of interest recorded.

Corresponding author: Ziqi Zhang, `ziqi.zhang@rochester.edu`

Abstract

The receiver function (RF) is a widely used crustal imaging technique. In principle, it assumes relatively noise-free traces that can be used to target receiver-side structures following source deconvolution. In practice, however, mode conversions and reflections may be severely degraded by noisy conditions, hampering robust estimation of crustal parameters. In this study, we use a sparsity-promoting Radon transform to decompose the observed RF traces into their wavefield contributions, i.e., direct conversions, multiples, and incoherent noise. By applying a crustal mask on the Radon-transformed RF, we obtain noise-free RF traces with only Moho conversions and reflections. We demonstrate, using a synthetic experiment and a real data example from the Sierra Nevada, that our approach can effectively de-noise the RFs and extract the underlying Moho signals. This greatly improves the robustness of crustal structure recovery as exemplified by subsequent $H - \kappa$ stacking. We further demonstrate, using a station sitting on loose sediments in the Upper Mississippi Embayment, that a combination of our approach and frequency-domain filtering can significantly improve crustal imaging in reverberant settings. We expect that our technique will enable high-resolution crustal imaging and inspire more applications of Radon transforms in seismic signal processing.

1 Introduction

The receiver function (RF) is a powerful seismic imaging technique for constraining crustal structure in various tectonic settings, e.g., orogenic belts (Parker et al., 2013; Yang et al., 2017), cratons (Thompson et al., 2010; Xia et al., 2017; Yuan, 2015), volcanoes (Leahy et al., 2010; Rychert et al., 2013), oceans (T. M. Olugboji et al., 2016), and even on other planets (Lognonné et al., 2020; Kim et al., 2021). Two ideas that are fundamental to using the technique include source deconvolution that targets receiver-side scattering (Ligorría & Ammon, 1999; Gurrola et al., 1995; Park & Levin, 2016) and modeling of the largest amplitude body-wave conversions and reflections generated from seismic discontinuities directly beneath the station (Wittlinger et al., 2009; Langston, 1979; Zandt & Ammon, 1995; Zhu & Kanamori, 2000; Julia et al., 2000; Bodin et al., 2013). During the modeling stage, e.g., $H - \kappa$ stacking and its various adaptations (Zhu & Kanamori, 2000; Wittlinger et al., 2009; Helffrich & Thompson, 2010; Rychert & Harmon, 2016), the RF traces are assumed to be relatively noise-free, permitting robust estimation of the crustal structure, i.e., crustal thickness (H) and P-to-S velocity ratio (κ). In practice, however, mode conversions and reflections may be severely degraded by noisy conditions. This may render the modeling step intractable, hampering robust estimation of the crustal parameters and the subsequent interpretation of crustal composition (Zandt & Ammon, 1995; Stankiewicz et al., 2002; Audet et al., 2009; He et al., 2013). For this reason, seismic analysts usually employ a variety of quality control procedures to select high-quality receiver functions, either manually or in an automated manner, e.g., using a combination of attributes from deconvolution, waveform features, and stacking statistics (Yang et al., 2016), or through supervised machine-learning models (Gong et al., 2022). Previous studies have also made several modifications to grid-search algorithms in an effort to improve the constraints from the low-amplitude reflections, including, but not limited to, using cluster analysis and semblance weighting (Philip Crotwell & Owens, 2005; Eaton et al., 2006), varying weighting factors for different phases (Vanacore et al., 2013), and performing moveout corrections preceding the grid-search (Rivadeneyra-Vera et al., 2019). In addition, several de-noising frameworks have been proposed to aid with the interpretation of noisy RF data, including transform-based methods (Q. Zhang et al., 2022; Chen et al., 2022; Q. Zhang et al., 2021; Chen et al., 2019; Dalai et al., 2019), rank-reduction techniques (Dokht et al., 2016; Rubio et al., 2020), and machine-learning frameworks (F. Wang et al., 2022; Dalai et al., 2021).

In this study, we de-noise the observed RF data using a modification of a recently proposed transform-based signal processing workflow, CRISP-RF (***C****lean* ***R****eceiver Function* ***I****maging using* ***SP****arse* ***R****adon* ***F****ilter*) (T. Olugboji et al., 2023). The central idea involves applying a sparse Radon transform to effectively decompose the Ps-RF into direct conversions, multiples, and noise, based on the time-slowness moveout and phase coherence. In our implementation here, we retain the crustal multiples as well as the direct arrivals generated at the Moho. We note that while our approach is illustrated using the traditional $H - \kappa$ stacking technique, it may be applied prior to data modeling using other grid search or waveform fitting techniques (Wittlinger et al., 2009; Helffrich & Thompson, 2010; Rychert & Harmon, 2016). The improvement in crustal imaging follows from noise suppression and enhanced detection of time-slowness arrivals of converted and reflected phases that enable robust back-projection during a crustal parameter search. We start by introducing the basic principles and processing steps of CRISP-RF, and what modifications are needed to suit our goal of preserving Moho conversions and multiples. We provide synthetic experiments and a real data example to demonstrate the effectiveness of our approach and to show that we are able to effectively de-noise the RF and improve the robustness of crustal structure estimation. We demonstrate using another data example that our approach can be coupled with resonance-filtering (Yu et al., 2015; Akuhara et al., 2016; Z. Zhang & Olugboji, 2021, 2023) to improve crustal imaging in reverberant settings.

2 Method

2.1 Brief Overview of Receiver Function and $H-\kappa$ Stacking

P-to-S receiver function (Ps-RF) is usually obtained by deconvolving the vertical component from the horizontal component seismograms, and targets receiver-side structure with the source and path removed (Langston, 1979; Ammon, 1991; Park & Levin, 2000; Zhong & Zhan, 2020). Assuming a simple laterally homogenous and horizontally layered model with a crust and a half-space, the Ps-RF trace should contain one direct conversion from the Moho (PmS) and two multiples (PPmS and PSmS) (Figure 1a). The $H-\kappa$ stacking method calculates the stacking amplitudes of Ps-RF traces of different slowness at the predicted arrival times of these phases using different pairs of H (crustal thickness) and κ (P-to-S velocity ratio) values and determines the optimal result by performing a grid search (Zhu & Kanamori, 2000):

$$s(H,\kappa) = \sum_i \sum_j w_j G(t_{ij}) R_j(t) \tag{1}$$

where s is the stacking amplitude, t_{ij} is the predicted arrival of the ith phase (i.e., PmS, PPmS, and PSmS), G is a Gaussian smoothing window centered at time t, R_j is the jth radial Ps-RF trace, and w_j is the weighting factors for different phases. In most implementations, the direct phase is weighted higher and the multiples are weighted lower due to their relative amplitudes (e.g., calculated from reflection and transmission coefficients in Z. Zhang and Olugboji (2021)). Here we use 0.4, 0.3, and -0.3 as the weighting factors for PmS, PPmS, and PSmS phases, respectively.

The predicted arrivals of each phase given a single-layer model with thickness H, compressional velocity v_p, and shear velocity v_s are given by

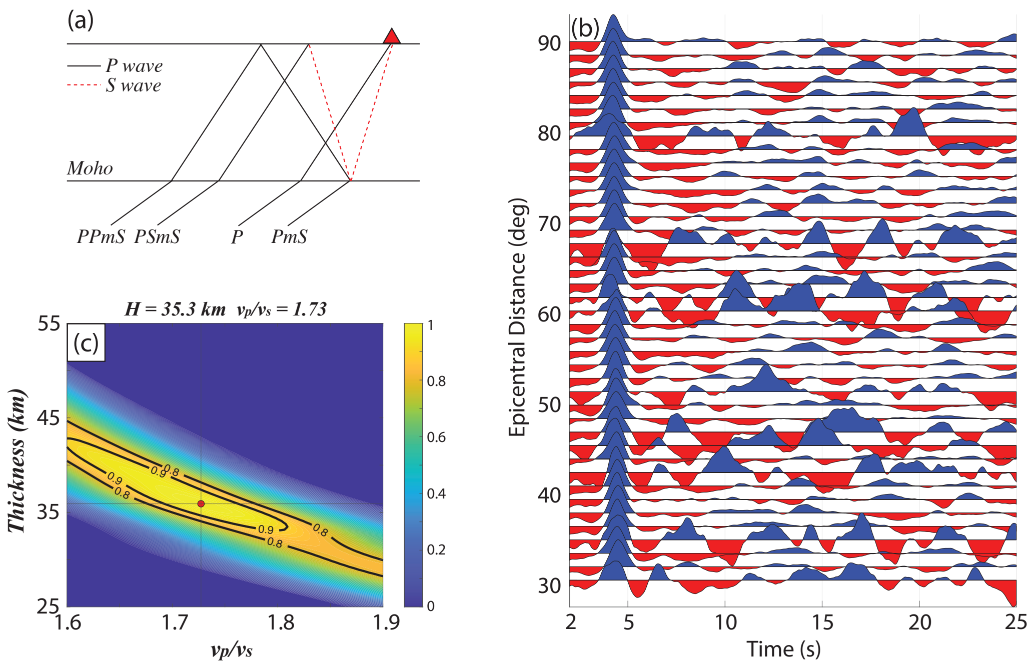

Figure 1. (a) Wave propagation of the direct P wave, direct P-to-S conversion at the Moho (PmS) and its multiples (PPmS and PSmS). (b) Synthetic Ps-RF traces of single-layer model plotted against epicentral distance. Amplitudes at later times are attenuated and random noise is added. (c) $H-\kappa$ stacking of the synthetic Ps-RF shown in (b). Black contour lines indicate 90% and 80% of the maximum stacking amplitude, respectively. For better visualization, we set all negative stacking amplitudes to zero.

$$t_{PmS} = H(\sqrt{\frac{1}{v_s^2} - p^2} - \sqrt{\frac{1}{v_p^2} - p^2}) \tag{2a}$$

$$t_{PPmS} = H(\sqrt{\frac{1}{v_s^2} - p^2} + \sqrt{\frac{1}{v_p^2} - p^2}) \tag{2b}$$

$$t_{PSmS} = 2H(\sqrt{\frac{1}{v_s^2} - p^2}) \tag{2c}$$

where p is the slowness of the Ps-RF trace.

Note that a crustal compressional velocity (v_p) is usually assumed in the $H-\kappa$ stacking so that the shear velocity (v_s) in Equation 2 can be substituted by $v_s = \frac{v_p}{\kappa}$. This a priori assumption is not necessary for some of the adaptations of the $H-\kappa$ stacking; e.g., Rychert and Harmon (2016) used both Ps- and Sp-RF in their stacking algorithm so that crustal parameters H, v_p, and v_s can be determined without assuming its elastic properties. Other examples include Kumar and Bostock (2008) which used least-squares regression to solve for v_p and κ and Helffrich and Thompson (2010) which improved the reliability of v_p and κ estimates when events with small slownesses are not available. Nevertheless, for simplicity, we illustrate our approach using the traditional $H-\kappa$ stacking technique.

2.2 Application of CRISP-RF: Sparse Radon Transform and Crustal Mask

2.2.1 CRISP-RF and Sparse Radon Transform

The slowness-binned Ps-RF stacks can be viewed as a 2-D matrix with one dimension representing the slowness (or epicentral distance in an 1-D earth model) and the other representing the time axis. Applying the Radon transform to this matrix allows us to describe the Ps-RF data, $\mathbf{d}$, by a sparse model set, $\mathbf{m}$:

$$\mathbf{d}(t,p) = \mathfrak{R}^\dagger\{\mathbf{m}(\tilde{\tau},q)\} \triangleq \sum_{i=1}^{N_q} \mathbf{m}(\tilde{\tau} = t - q_i p^2, q_i) \tag{3}$$

where $\mathbf{d}(t,p)$ is the Ps-RF data in the time-slowness domain, $\mathbf{m}(\tilde{\tau},q)$ is the Radon model in the intercept-time-curvature domain (here intercept-time refers to the arrival time assuming zero slowness, and curvature refers to the extent of the moveout of the phases), and $\mathfrak{R}^\dagger$ is the adjoint Radon transform. Ideally, the Radon model ($\mathbf{m}$) should only have non-zero amplitudes at intercept-time and curvature pairs corresponding to coherent arrival phases,

Table 1. Detailed $H-\kappa$ stacking results of synthetic experiments and real data examples

Case	Figure(s)	H_{raw}* (km)	H_{filtered}* (km)	H Improvement*	κ_{raw}*	κ_{filtered}*	κ Improvement*
Synthetic	1, 2, 4	$35.3^{+7.58}_{-2.12}$	$35.0^{+1.53}_{-1.30}$	67%	$1.73^{+0.079}_{-0.130}$	$1.75^{+0.061}_{-0.056}$	44%
WCN	6	$35.3^{+2.95}_{-2.43}$	$35.9^{+1.45}_{-1.78}$	40%	$1.72^{+0.090}_{-0.087}$	$1.69^{+0.070}_{-0.055}$	29%
HENM	7	$34.0^{+1.14}_{-2.26}$	$34.0^{+1.49}_{-1.61}$	38%	$1.85^{+0.125}_{-0.108}$	$1.85^{+0.073}_{-0.062}$	42%

* H, κ_{raw} and $H, \kappa_{\text{filtered}}$ denotes the optimal solution and the 90% error range of the $H-\kappa$ stacking results of raw Ps-RF and filtered Ps-RF from the adjoint Radon transform, respectively. H, κ Improvement denotes the percentage decreased in the 90% error range of $H, \kappa_{\text{filtered}}$ compared to H, κ_{raw}. In the case of station HENM, H, κ_{raw} corresponds to the $H-\kappa$ stacking on the Ps-RF after resonance filtering (Figure 7d).

i.e., PmS, PPmS, and PSmS in the single-layer scenario. The adjoint Radon transform, $\mathfrak{R}^{\dagger}$, reconstructs the Ps-RF data ($\mathbf{d}$) by summing the amplitudes of the Radon model at all curvature (q_i) along each slowness (p).

The CRISP-RF workflow starts by applying a sparsity-promoting Radon transform that effectively decomposes the input Ps-RF data into direct conversions, multiple reflections, and incoherent noise (T. Olugboji et al., 2023). Here, we demonstrate the performance of the sparsity-promoting Radon transform for noise suppression using a synthetic Ps-RF generated for a single-layer model with a crustal thickness of 35 km, a compressional velocity of 6.3 km/s, and a shear velocity of 3.6 km/s. To mimic the behavior of noisy realistic data, we attenuate the amplitudes (100% to 10%) of the late arriving multiples ($0 < t < 12$ s) and then add realistic noise with a signal-to-noise ratio (SNR) of 2.0 to all the traces. We then add noise with a significantly lower SNR of 0.5 to 10 randomly chosen traces, resulting in a noisy dataset with low amplitude multiples whose arrivals are hard to visually identify (Figure 1b). Applying the $H-\kappa$ stacking on this Ps-RF resolves a Moho depth of 35.3 km and a P-to-S velocity ratio of 1.73 (Figure 1c; see Table 1 for the 90% error range). The sparse Radon model calculated from the CRISP-RF workflow shows a clear separation of the three Moho-related phases, with the direct conversion being the strongest positive phase mapped into the positive curvature domain, the first multiple (PPmS) mapped into the negative curvature domain with a positive amplitude, and the second multiple (PSmS) also in the negative curvature domain but with a negative amplitude (Figure 2).

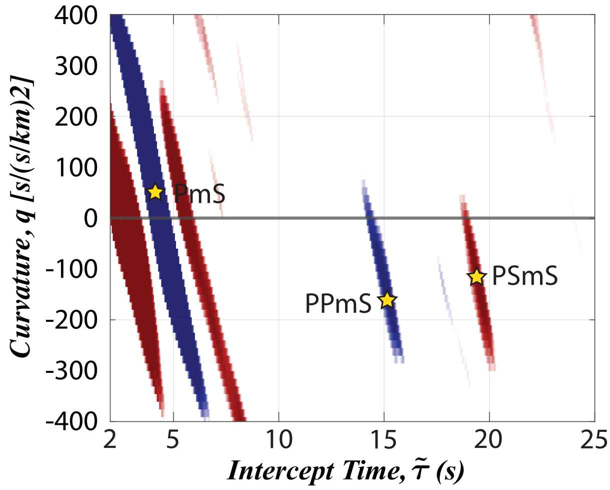

Figure 2. Sparse Radon model of the synthetic Ps-RF shown in Figure 1b obtained from the CRISP-RF workflow. Stars denote the theoretical $(\tilde{\tau}, q)$ locations of the Moho phases calculated from Equation 4(b, d, f).

2.2.2 Keeping Moho Phases: Crustal Mask

Following the sparsity-promoting Radon transform that maps different arrivals into their corresponding intercept-time-curvature locations in the Radon image, a masking filter is applied to only retain the Moho-related phases (it is here that CRISP-RF differs from its initial goal of being used to filter out crustal multiples). The Radon-transformed and filtered RFs are effectively de-noised due to the sparsity-promoting step.

The key to designing this masking filter is to determine a plausible 2-D window for the intercept-time-curvature parameters that contain the phases of interest. As introduced earlier, intercept-time $(\tilde{\tau})$ refers to the phase arrival assuming zero slowness, i.e., by substituting $p = 0$ in Equation 2, and the curvature (q) is the degree-two coefficient of the quadratic polynomial of the Taylor expansion of Equation 2 (Ryberg & Weber, 2000; J. Shi et al., 2020; T. Olugboji et al., 2023):

$$t_{PmS} = \tilde{\tau}_{PmS} + q_{PmS}p^2 \tag{4a}$$

$$\tilde{\tau}_{PmS} = H\left(\frac{1}{v_s} - \frac{1}{v_p}\right) \qquad q_{PmS} \approx +\frac{H(v_p - v_s)}{2} \tag{4b}$$

$$t_{PPmS} = \tilde{\tau}_{PPmS} + q_{PPmS}p^2 \tag{4c}$$

$$\tilde{\tau}_{PPmS} = H\left(\frac{1}{v_s} + \frac{1}{v_p}\right) \qquad q_{PPmS} \approx -\frac{H(v_p + v_s)}{2} \tag{4d}$$

$$t_{PSmS} = \tilde{\tau}_{PSmS} + q_{PSmS}p^2 \tag{4e}$$

$$\tilde{\tau}_{PSmS} = 2H\frac{1}{v_s} \qquad q_{PSmS} \approx -Hv_s \tag{4f}$$

The crustal masking filter for the intercept-time ($\tilde{\tau}$) and curvature (q) is obtained by substituting the grid-search parameter bounds into Equation 4(b, d, f), e.g., for a generic crustal velocity model, H = 25 - 55 km, v_p = 6.3 km/s and v_s = 3.6 km/s. This results in three distinct line segments in the intercept-time-curvature domain, one in the positive-curvature half (PmS) and two in the negative-curvature half (PPmS and PSmS). To account for the numeric errors along the curvature axis during the Radon transform, we further add a tolerance width to the line segments, resulting in a crustal mask that passes through both direct and multiple phases for a given range of depth (Figure 3). The rectangular areas of PmS and PPmS phases only pass through positive amplitudes, and that of PSmS phases only passes through negative amplitudes, in accordance with the phase polarities of each respective phase.

We apply this crustal mask to the previously calculated sparse Radon model and perform the adjoint Radon transform to obtain a noise-free filtered Ps-RF, which shows significantly enhanced detections of the Moho multiples (Figure 4a). Consequently, the $H-\kappa$ stacking shows a better constraint on the crustal structure, resolving a Moho depth of 35.0 km and a velocity ratio of 1.75 (Figure 4b; see Table 1 for the 90% error range). This result matches the input model perfectly, and shows a 67% narrower error range on H and 44% on κ, respectively, compared to the $H-\kappa$ stacking directly on the raw synthetic Ps-RF (compare Figure 4b with Figure 1c; see also Table 1). The 80% error range of the $H-\kappa$ stacking on the filtered Ps-RF is from 32.43 to 37.48 km for H and from 1.670 to 1.841 for κ, which is even narrower than the 90% error range of the $H-\kappa$ stacking on the raw Ps-RF, while the 80% error range of the $H-\kappa$ stacking on the raw Ps-RF is outside the search range (compare Figures 1c and 4b). This improvement largely comes from the better

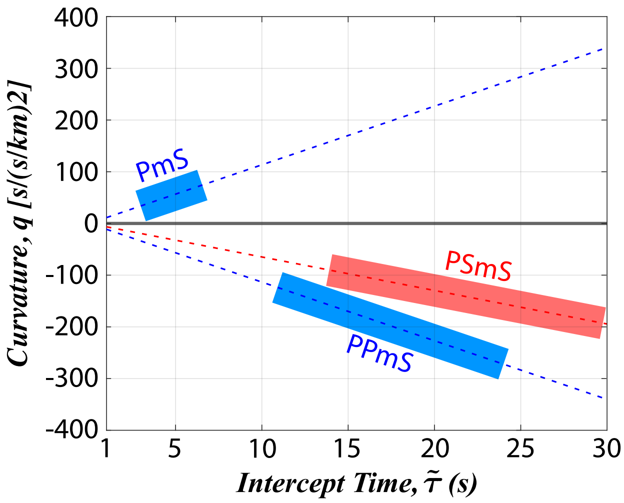

Figure 3. Masking filter designed to only pass through Moho-related phases in the Radon image. Dashed lines indicate the predicted intercept-time-curvature curves for each given phase; colored rectangles indicate the final pass-through areas in the mask obtained by limiting the Moho depth and adding a tolerance width. Red and blue colors indicate positive and negative arrivals, respectively.

constraint from the multiples (PPmS and PSmS), which is made possible by the de-noising effect provided by the CRISP-RF.

2.3 *H-k* Stacking on Radon Image

The Radon image is an intercept-time-curvature domain representation of the Ps-RF data, therefore the $H-\kappa$ stacking can also be applied to the Radon image directly before transforming it back to the time-slowness domain. Similar to the traditional $H-\kappa$ stacking, given a pair of (H, κ) values, one can calculate the corresponding ($\tilde{\tau}$, q) values for the three phases (PmS, PPmS, and PSmS) from the middle and right columns of Equation 4. A 2-D weighting matrix can then be constructed with only non-zero elements being the 2-D elliptical Gaussians centered at these three calculated ($\tilde{\tau}$, q) locations (e.g., Figure 5). The $H-\kappa$ stacking on the Radon image is thus conducted by a grid search of the (H, κ) pairs to maximize the stacking amplitude obtained by the element-wise product of the weighting matrix and the Radon image. This also resolves the crustal structure perfectly, and shows a similar stacking image as the one applied to the time-epicentral-distance domain Ps-RF, although with a slightly larger 90% error range (33.01 to 36.79 km for H and 1.687 to 1.817 for κ) (Figure 5b).

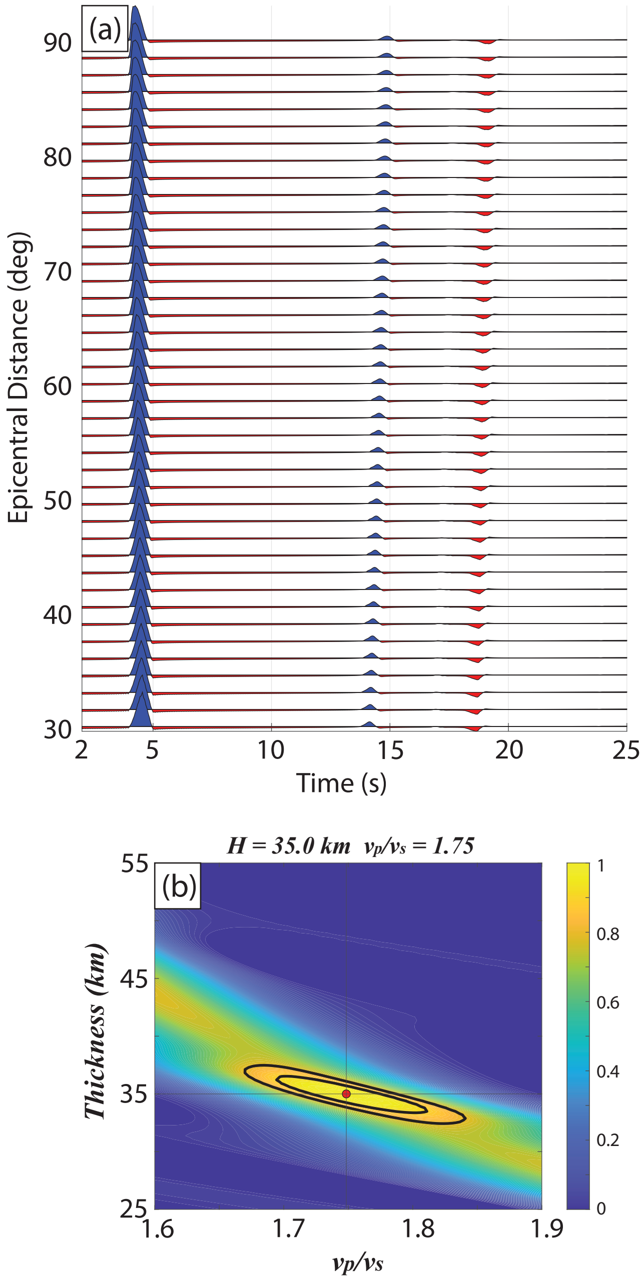

Figure 4. (a) Filtered Ps-RF obtained from the adjoint Radon transform of the Radon image shown in Figure 2 after applying the crustal mask shown in Figure 3. (b) $H - \kappa$ stacking of the filtered Ps-RF shown in (a). Black contour lines indicate 90% and 80% of the maximum stacking amplitude, respectively.

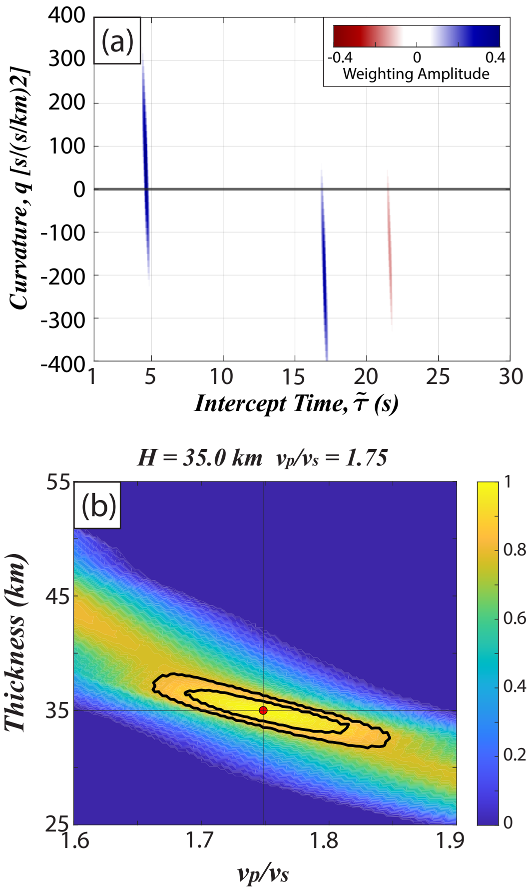

Figure 5. (a) Example of a 2-D weighting matrix constructed using $H = 40$ km and $\kappa = 1.7$. (b) $H - \kappa$ stacking of the Radon image shown in Figure 2. Black contour lines indicate 90% and 80% of the maximum stacking amplitude, respectively.

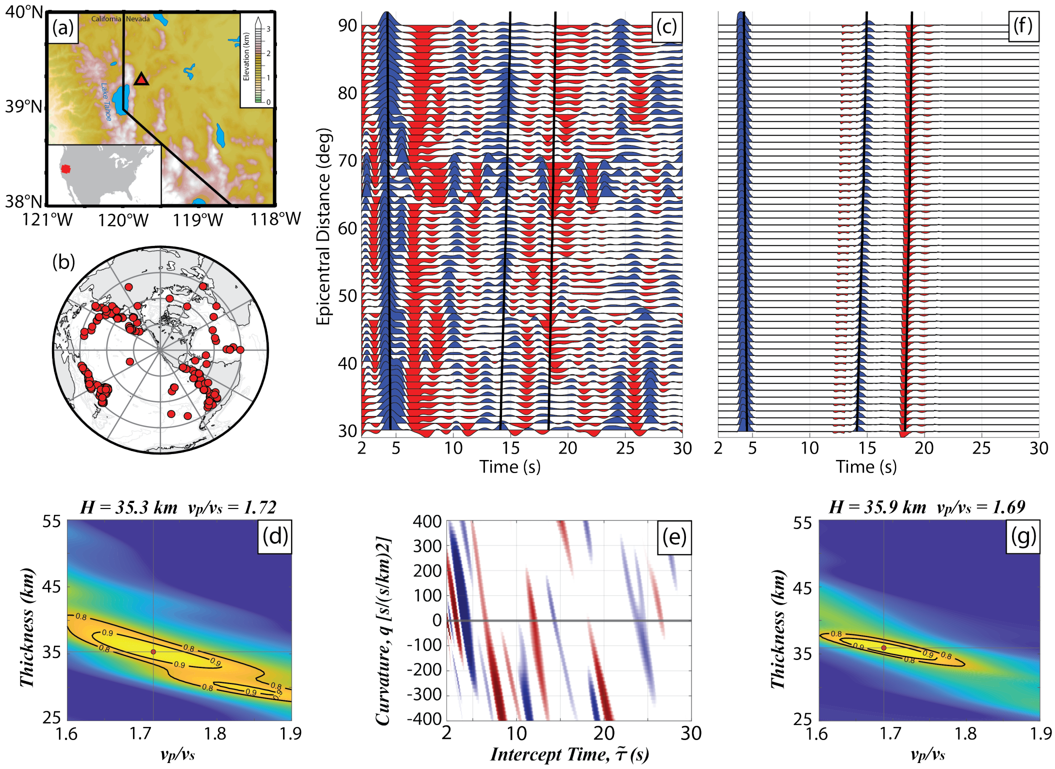

Figure 6. (a) Location and geological settings of station WCN. Red triangle indicates the station location. the bottom-left inset map shows the location of the study area relative to the contiguous US. (b) Location of the teleseismic events used in the receiver function calculation. (c) Raw Ps-RF traces calculated at station WCN plotted against epicentral distance. Black vertical lines indicate the predicted arrival times of the PmS, PPmS, and PSmS phases calculated from the optimal $H-\kappa$ solution. (d) $H-\kappa$ stacking of the raw Ps-RF shown in (c). Black contour lines are 90% and 80% of the maximum stacking amplitude as indicated. (d) Sparse Radon model of the raw Ps-RF shown in (c) obtained from the CRISP-RF workflow. (f) Filtered Ps-RF traces obtained from the adjoint Radon transform of the Radon image shown in (e) after applying the crustal mask shown in Figure 3. (g) $H-\kappa$ stacking of the filtered Ps-RF shown in (f).

3 Application to Data

In this section, we apply the CRISP-RF signal de-noising approach to station WCN located in the mid-northern section of Sierra Nevada, to the northeast of Lake Tahoe (Figure 6a). Located in the Great Valley forearc basin, this station sits on complicated crustal structures including metamorphosed ophiolites, Mesozoic-age arc-related plutons, Cenozoic-age volcanic deposits, and extensional grabens associated with sedimentation along the Basin and Range boundary(Frassetto et al., 2010). This diversity of crustal composition could likely lead to a complex teleseismic wavefield and hard-to-detect Moho multiples, making it an ideal location to test the effectiveness of our approach on real seismic data.

We obtain 235 high-quality (SNR > 2.0) teleseismic events (Mw > 6.0, $30° < \Delta < 90°$; Figure 6b) and calculate the Ps-RF traces at the cut-off frequency of 1.0 Hz using the extended-time multi-taper approach (Park & Levin, 2000; Helffrich, 2006; Shibutani et al., 2008). We stack the Ps-RFs every 1° with 8 ° overlapping epicentral distance bins (Figure 6c). We use a P wave velocity of 6.3 km/s in the $H - \kappa$ stacking at this station following K. Wang et al. (2022). The raw Ps-RF image shows a clear direct conversion from the Moho just before 5 s, and various other pulses, some of which exhibit coherence across different epicentral distances while others do not. Upon further visual inspection, a positive phase with a negative moveout can be roughly observed at around 15 s as the PPmS multiple; the arrival of the PSmS multiple is harder to determine as there are several negative phases between 15 and 20 s. Applying $H - \kappa$ stacking on the raw Ps-RF resolves a crustal thickness of 35.3 km and a P-to-S velocity ratio of 1.72 (Figure 6d). This $H - \kappa$ image displays two local maxima (as defined by the 90% error range contours), indicating ambiguous stacking results due to noisy Ps-RF traces and poor constraints from multiple phases. For the local maxima at the optimal solution, the 90% error range is from 32.87 to 38.25 km for H and from 1.633 to 1.810 for κ, while the 80% error contour is outside the search range.

We then apply the CRISP-RF workflow on the raw Ps-RF to obtain its sparse Radon model (Figure 6e). Although the Radon image shows more phases and is more complex compared to the synthetic one (Figure 2) due to the complicated crustal structure detected in real seismic data, the adjoint Radon transform after applying the crustal mask gives a clean Ps-RF image with clearly identified direct conversion (PmS at ~ 5 s) and multiple reflections (PPmS at ~ 15 s and PSmS at ~ 18 s) from the Moho (Figure 6f). Consequently, the $H - \kappa$ stacking of the filtered Ps-RF traces resolves the crustal structure with far less ambiguity, with a crustal thickness of 35.9 km and a P-to-S velocity ratio of 1.69 (Figure 6g). This $H - \kappa$ image shows only one maxima, with the 90% error range of H and κ 40% and 29% narrower, respectively, compared to the $H - \kappa$ stacking directly on the raw Ps-RF (compare Figures 6d and 6e; see also Table 1). The 80% error range of the $H - \kappa$ stacking on the filtered Ps-RF is from 33.17 to 38.05 km for H and from 1.610 to 1.798 for κ, which is at least 59% and 37% narrower than that on the raw Ps-RF, and is comparable to the 90% error range of the $H - \kappa$ stacking on the raw Ps-RF.

4 Discussion

4.1 Crustal Imaging Through Complicated Structures: Promises and Limitations

In this study, we introduce modifications to the CRISP-RF workflow introduced by T. Olugboji et al. (2023) to extract Moho phases and suppress background noise using spare Radon transforms, and show that this improves the quality of crustal imaging through $H-\kappa$ stacking. While our proposed approach is proven effective by both a synthetic experiment and a real data example, it is based on the assumption that the Ps-RF traces are not contaminated by any significant signal-generated noise, i.e., reverberations. Reverberations coming from sedimentary, oceanic, or glacial layers could generate high-amplitude resonant noise in the Ps-RF traces due to their low seismic velocity, completely masking conversion and reflection phases from the Moho and even deeper discontinuities (Yeck et al., 2013; Yu et al., 2015; Audet, 2016; Chai et al., 2017; Cunningham & Lekic, 2019; Z. Zhang & Gao, 2019). Since the Ps-RF traces calculated at stations above such reverberant environments are dominated by a resonance that resembles a decaying sinusoid, the proposed approach in this study will likely fail because the distinct, time-separated, and coherent arrivals are no longer present. A systematic data-driven approach, FADER (***FA****st* ***D****etection and* ***E****limination of Echoes and* ***R****everberations*), has recently been proposed by Z. Zhang and Olugboji (2023) to solve the twin problem of detection and elimination of reverberations without a priori knowledge of the elastic structure of the reverberant layers. This approach uses autocorrelation and cepstral analysis to extract the signature of reverberation and then uses a frequency domain filter to remove it and obtain reverberation-free Ps-RF. Therefore, it is natural to combine both techniques to achieve a better crustal image in reverberant settings.

To demonstrate the possibility of applying our proposed approach after filtering out reverberation, we select station HENM located in the Upper Mississippi Embayment, where loose sediments are widely present (Figure 7a). We obtain 192 high-quality (SNR $>$ 2.0) teleseismic events (Mw $>$ 6.0, $30^\circ < \Delta < 90^\circ$; Figure 7b) and calculate the Ps-RF traces using the same method and parameters described earlier. We use a P wave velocity of 6.1 km/s in the $H-\kappa$ stacking at this station following Liu et al. (2017). The raw Ps-RF traces show strong reverberant behavior, with no clearly identified phases (Figure 7c), and therefore lead to a poorly constrained $H-\kappa$ stacking image with multiple local maxima and an optimal stacking solution at the boundary of the search range (Figure 7g). Applying

FADER effectively eliminates the resonant noise in the Ps-RF traces, making the direct conversion from the Moho clearly visible at around 5 s, along with the two multiple phases at around 14 s and 17 s, respectively, although not as coherent (Figure 7d). This results in a much better constrained $H-\kappa$ stacking image, with an optimal solution of 34.0 km for H and 1.85 for κ (Figure 7h; see Table 1 for the 90% error range). Applying the proposed approach in this study further eliminates all phases and background noise except for the Moho phases, resulting in a clean, noise-free Ps-RF image (Figure 7e). The consequent $H-\kappa$ stacking gives the same solution of $H = 34.0$ km and $\kappa = 1.85$, with an even narrow 90% error range (38% narrower for H and 42% narrower for κ) (compare Figures 7h and 7i; see also Table 1).

We note that shallow layer reverberations commonly observed in geological settings like sediments, oceans, and glaciers are a special complicating case where near-surface crustal structure hampers the reliability of Ps-RF imaging results. Other cases include a crust-to-mantle transition that is gradational or a complex crustal structure, e.g., dipping Moho, intra-crustal layers, and crustal anisotropy (Frederiksen & Bostock, 2000; Ogden et al., 2019; Y. Shi et al., 2023). In all these cases, the crustal properties deviate from the simple case considered in our synthetic experiments (a single layer with a sharp Moho), and therefore the $H-\kappa$ stacking may give unreliable results. Under these circumstances, we recommend caution when applying our proposed approach due to the difficulty of interpreting a more complicated Radon image.

4.2 Improving Constraints on Crustal Composition and Evolution

P-to-S velocity ratio (κ) can be directly converted to Poisson's ratio (σ) (Christensen & Fountain, 1975):

$$\sigma = 0.5\left[1 - \frac{1}{\kappa^2 - 1}\right] \tag{5}$$

Improved resolution of κ following denoising provides much tighter constraints on the inferred crustal composition, providing important information on the geological evolution of the Earth's crust (Zandt & Ammon, 1995; Stankiewicz et al., 2002; Guo et al., 2019). For instance, an increase in plagioclase content and a decrease in quartz can increase the Poisson's ratio from 0.24 for a granitic rock to 0.27 for a diorite, and to 0.30 for a gabbro (Tarkov & Vavakin, 1982).

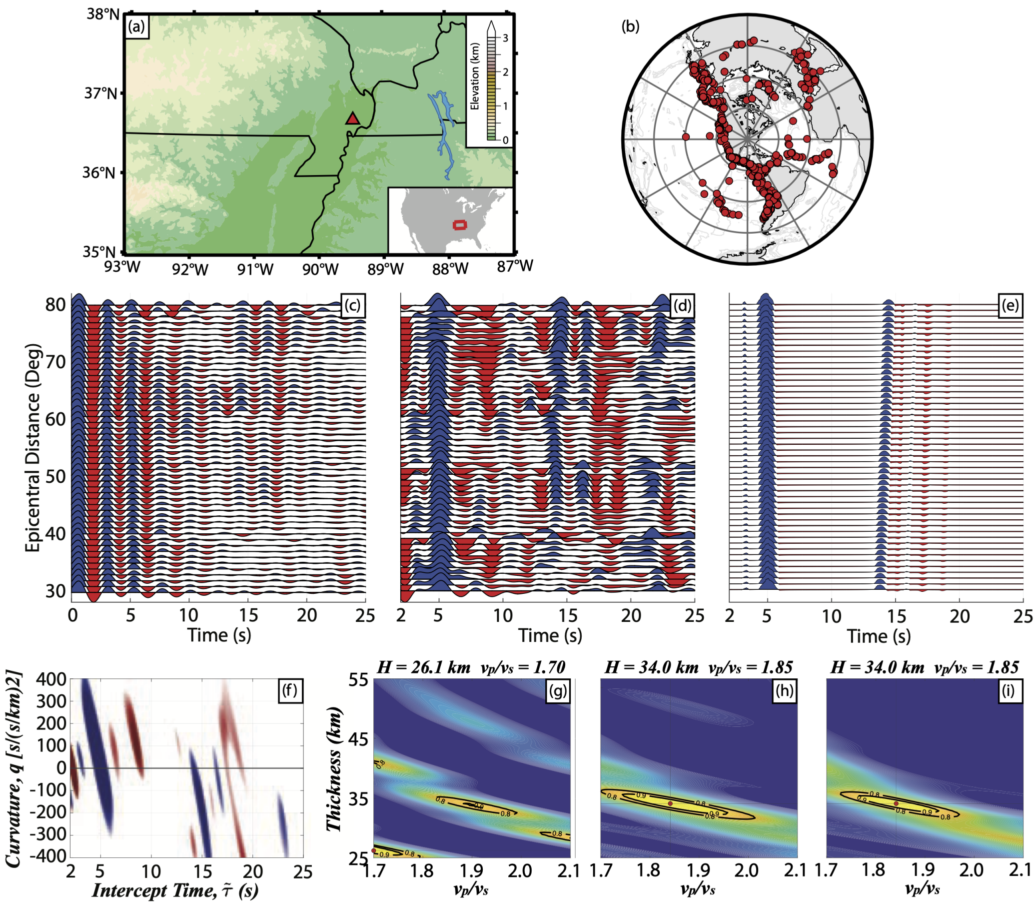

Figure 7. (a) Location and geological settings of station HENM. Red triangle indicates the station location. the bottom-right inset map shows the location of the study area relative to the contiguous US. (b) Location of the teleseismic events used in the receiver function calculation. (c) Raw Ps-RF traces calculated at station WCN plotted against epicentral distance. (d) Ps-RF traces after reverberation removal. (e) Ps-RF traces after reverberation removal and applying the modified CRISP-RF workflow. (f) Sparse Radon model of the raw Ps-RF shown in (d) obtained from the CRISP-RF workflow. (g) $H-\kappa$ stacking of the raw Ps-RF shown in (c). (h) $H-\kappa$ stacking of the processed Ps-RF shown in (d). (i) $H-\kappa$ stacking of the processed Ps-RF shown in (e).

Receiver function imaging studies have routinely used this sensitivity of crustal composition to Poisson's ratio to study how bulk composition varies for different geological terranes. For example, thanks to the massive high-quality seismic data from USArray and EARS (Philip Crotwell & Owens, 2005), Lowry and Pérez-Gussinyé (2011) proposed a feedback mechanism where ductile strain first localizes quartz-rich, weak crust, leading to processes that promote advective warming, hydration, and further weakening, based on the correlation between low Poisson's ratios, higher lithospheric temperatures, and deformation in the Cordillera region. Similarly, Ma and Lowry (2017) estimated the seismic velocity ratios across the continent U.S. and suggested Cordilleran high heat flow may partly reflect crustal hydration enthalpy. Other examples include Audet et al. (2009) which implied high pore-fluid pressures and thus an overpressured subducted oceanic crust at northern Cascadia indicated by anomalously high Poisson's ratio and He et al. (2013) which suggested a dominantly felsic lower crust and the presence of lower crustal delamination in the Cathaysia Block in Southern China from the low Poisson's ratio.

The reliability of these interpretations depends heavily on the accuracy of the P-to-S velocity ratio (κ) estimation. We have shown that by de-noising the Ps-RF using our proposed approach, the measurement error for κ in the traditional $H-\kappa$ stacking can be greatly reduced (Table 1), enabling more robust estimation of crustal structures.

4.3 Application of Radon Transform in Seismic Signal Processing

We have applied a sparse Radon transform in high-resolution Ps-RF imaging of sharp discontinuities. As we have demonstrated above, this data processing technique can be beneficial not only when imaging upper mantle discontinuities as suggested by T. Olugboji et al. (2023), but also for improved detection of multiple reflected phases when imaging the crust. The Radon transform maps the coherent phases in the time-domain Ps-RF traces onto the Radon model based on their moveout and amplitudes. The same philosophy is also applicable to other seismic imaging techniques, e.g., top- and bottom-side reflections, since each arriving phase also follows a distinct moveout (Gu et al., 2009; Gu & Sacchi, 2009). In these cases, modifications to Equations 2, 3, 4 are needed as the theoretical arrivals in these observations are different and their relationship with slowness or epicentral distance may be different (e.g., linear instead of parabolic).

5 Conclusion

In this study, we use a sparsity-promoting Radon transform to decompose the Ps-RF into its scattered wave contributions, i.e., direct conversions, multiples, and incoherent noise. By applying a specially designed crustal mask to the Radon model and transforming the now filtered Ps-RFs into the time domain using an adjoint Radon transform, a set of clean, noise-free Ps-RF traces is obtained. This leads to robust interpretations of crustal structure. This technique for crustal imaging using Ps-RFs is a modification to the CRISP-RF workflow proposed by T. Olugboji et al. (2023), which originally targets upper mantle discontinuities. We demonstrate, using both synthetic experiments and real data examples, that our approach can effectively de-noise the Ps-RF traces and extract all Moho phases, and therefore greatly reduce the error range in the grid search for crustal parameters. We also demonstrate the CRISP-RF de-noising with a simultaneous de-reverberation technique proposed by Z. Zhang and Olugboji (2021, 2023), which improves crustal imaging beneath reverberant layers. We anticipate our approach will enable high-resolution crustal imaging with noisy teleseismic receiver functions and inspire more applications of the sparse Radon transform for seismic imaging.

6 Data and Resources

All seismic data used in this study can be obtained from the IRIS Data Management Center (`https://ds.iris.edu/ds`) under the network codes NN (station WCN) and NM (station HENM). Synthetic receiver functions were computed using the Telewavesim open-source Python library provided by (Audet et al., 2019). The extended-time multi-taper deconvolution program and the CRISP-RF data processing workflow are provided by (T. Olugboji et al., 2023) and can be retrieved from the open-source repository at `https://doi.org/10.5281/zenodo.7996504`.

7 Acknowledgments

This work was made possible by the support from the National Science Foundation under grant number: 1818654. The authors acknowledge the use of the BlueHive Linux cluster at the University of Rochester's Center for Integrated Research Computing, CIRC (`https://www.circ.rochester.edu/`).

References

Akuhara, T., Mochizuki, K., Kawakatsu, H., & Takeuchi, N. (2016, September). Nonlinear waveform analysis for water-layer response and its application to high-frequency receiver function analysis using OBS array. *Geophysical Journal International*, *206*(3), 1914–1920. doi: 10.1093/gji/ggw253

Ammon, C. J. (1991). The isolation of receiver effects from teleseismic P waveforms. *Bulletin-Seismological Society of America*, *81*(6), 2504–2510.

Audet, P. (2016, June). Receiver functions using OBS data: promises and limitations from numerical modelling and examples from the cascadia initiative. *Geophysical Journal International*, *205*(3), 1740–1755. doi: 10.1093/gji/ggw111

Audet, P., Bostock, M. G., Christensen, N. I., & Peacock, S. M. (2009, January). Seismic evidence for overpressured subducted oceanic crust and megathrust fault sealing. *Nature*, *457*(7225), 76–78. doi: 10.1038/nature07650

Audet, P., Thomson, C., Bostock, M., & Eulenfeld, T. (2019, December). Telewavesim: Python software for teleseismic body wave modeling. *Journal of open source software*, *4*(44), 1818. doi: 10.21105/joss.01818

Bodin, T., Yuan, H., & Romanowicz, B. (2013, November). Inversion of receiver functions without deconvolution—application to the indian craton. *Geophysical Journal International*, *196*(2), 1025–1033. doi: 10.1093/gji/ggt431

Chai, C., Ammon, C. J., Anandakrishnan, S., Ramirez, C., & Nyblade, A. (2017, February). Estimating subglacial structure using p-wave receiver functions. *Geophysical Journal International*, *209*(2), 1064–1079. doi: 10.1093/gji/ggx075

Chen, Y., Chen, J., Guo, B., Qi, S., & Zhao, P. (2019). Denoising the receiver function through curvelet transforming and migration imaging. *Chinese Journal of Geophysics*, *62*(6), 2027–2037.

Chen, Y., Gu, Y. J., Zhang, Q., Wang, H., Zuo, P., & Chen, Y. (2022, September). *Least-squares migration imaging of receiver functions.* doi: 10.1002/essoar.10512413.1

Christensen, N. I., & Fountain, D. M. (1975, February). Constitution of the lower continental crust based on experimental studies of seismic velocities in granulite. *GSA Bulletin*, *86*(2), 227–236. doi: 10.1130/0016-7606(1975)86⟨227:COTLCC⟩2.0.CO;2

Cunningham, E., & Lekic, V. (2019, October). Constraining crustal structure in the presence of sediment: a multiple converted wave approach. *Geophysical Journal International*, *219*(1), 313–327. doi: 10.1093/gji/ggz298

Dalai, B., Kumar, P., Srinu, U., & Sen, M. K. (2021, December). De-noising receiver function data using the unsupervised deep learning approach. *Geophysical Journal International*, *229*(2), 737–749. doi: 10.1093/gji/ggab494

Dalai, B., Kumar, P., & Yuan, X. (2019, March). De-noising receiver function data using the seislet transform. *Geophysical Journal International*, *217*(3), 2047–2055. doi: 10.1093/gji/ggz135

Dokht, R. M. H., Gu, Y. J., & Sacchi, M. D. (2016, December). Singular spectrum analysis and its applications in mapping mantle seismic structure. *Geophysical Journal International*, *208*(3), 1430–1442. doi: 10.1093/gji/ggw473

Eaton, D. W., Dineva, S., & Mereu, R. (2006, June). Crustal thickness and VP/VS variations in the grenville orogen (ontario, canada) from analysis of teleseismic receiver functions. *Tectonophysics*, *420*(1), 223–238. doi: 10.1016/j.tecto.2006.01.023

Frassetto, A., Zandt, G., Gilbert, H., Owens, T. J., & Jones, C. H. (2010, July). Improved imaging with phase-weighted common conversion point stacks of receiver functions. *Geophysical Journal International*, *182*(1), 368–374. doi: 10.1111/j.1365-246X.2010.04617.x

Frederiksen, A. W., & Bostock, M. G. (2000, May). Modelling teleseismic waves in dipping anisotropic structures. *Geophysical Journal International*, *141*(2), 401–412. doi: 10.1046/j.1365-246x.2000.00090.x

Gong, C., Chen, L., Xiao, Z., & Wang, X. (2022). Deep learning for quality control of receiver functions. *Frontiers in Earth Science*, *10*. doi: 10.3389/feart.2022.921830

Gu, Y. J., An, Y., Sacchi, M., Schultz, R., & Ritsema, J. (2009). Mantle reflectivity structure beneath oceanic hotspots. *Geophysical Journal International*, *178*(3), 1456–1472.

Gu, Y. J., & Sacchi, M. (2009, October). Radon transform methods and their applications in mapping mantle reflectivity structure. *Surveys in Geophysics*, *30*(4), 327–354. doi: 10.1007/s10712-009-9076-0

Guo, L., Gao, R., Shi, L., Huang, Z., & Ma, Y. (2019, March). Crustal thickness and poisson's ratios of south china revealed from joint inversion of receiver function and gravity data. *Earth and planetary science letters*, *510*, 142–152. doi: 10.1016/j.epsl.2018.12.039

Gurrola, H., Baker, G. E., & Minster, J. B. (1995, March). Simultaneous time-domain deconvolution with application to the computation of receiver functions. *Geophysical Journal International*, *120*(3), 537–543. doi: 10.1111/j.1365-246X.1995.tb01837.x

He, C., Dong, S., Santosh, M., & Chen, X. (2013). Seismic evidence for a geosuture between the yangtze and cathaysia blocks, south china. *Scientific reports*, *3*, 2200. doi: 10.1038/srep02200

Helffrich, G. (2006, February). Extended-Time multitaper frequency domain Cross-Correlation Receiver-Function estimation. *Bulletin of the Seismological Society of America*, *96*(1), 344–347. doi: 10.1785/0120050098

Helffrich, G., & Thompson, D. (2010, June). A stacking approach to estimate VP/VS from receiver functions: Stacking to estimate VP/VS. *Geophysical Journal International*, *182*(2), 899–902. doi: 10.1111/j.1365-246X.2010.04628.x

Julia, J., Ammon, C. J., Herrmann, R. B., & Correig, A. M. (2000). Joint inversion of receiver function and surface wave dispersion observations. *Geophysical Journal International*, *143*(1), 99–112.

Kim, D., Lekić, V., Irving, J. C. E., Schmerr, N., Knapmeyer-Endrun, B., Joshi, R., ... Banerdt, W. B. (2021, November). Improving constraints on planetary interiors with PPs receiver functions. *Journal of geophysical research. Planets*, *126*(11), e2021JE006983. doi: 10.1029/2021JE006983

Kumar, M. R., & Bostock, M. G. (2008, November). Extraction of absolute P velocity from receiver functions. *Geophysical Journal International*, *175*(2), 515–519. doi: 10.1111/j.1365-246X.2008.03963.x

Langston, C. A. (1979). Structure under mount rainier, washington, inferred from teleseismic body waves. *Journal of geophysical research*, *84*(B9), 4749. doi: 10.1029/JB084iB09p04749

Leahy, G. M., Collins, J. A., Wolfe, C. J., Laske, G., & Solomon, S. C. (2010, October). Underplating of the hawaiian swell: evidence from teleseismic receiver functions. *Geophysical Journal International*, *183*(1), 313–329. doi: 10.1111/j.1365-246X.2010.04720.x

Ligorría, J. P., & Ammon, C. J. (1999, October). Iterative deconvolution and receiver-function estimation. *Bulletin of the Seismological Society of America*, *89*(5), 1395–1400. doi: 10.1785/BSSA0890051395

Liu, L., Gao, S. S., Liu, K. H., & Mickus, K. (2017, June). Receiver function and gravity constraints on crustal structure and vertical movements of the upper mississippi embayment and ozark uplift. *Journal of Geophysical Research, [Solid Earth]*, *122*(6), 4572–4583. doi: 10.1002/2017jb014201

Lognonné, P., Banerdt, W. B., Pike, W. T., Giardini, D., Christensen, U., Garcia, R. F.,

… Zweifel, P. (2020, February). Constraints on the shallow elastic and anelastic structure of mars from InSight seismic data. *Nature geoscience*, *13*(3), 213–220. doi: 10.1038/s41561-020-0536-y

Lowry, A. R., & Pérez-Gussinyé, M. (2011, March). The role of crustal quartz in controlling cordilleran deformation. *Nature*, *471*(7338), 353–357. doi: 10.1038/nature09912

Ma, X., & Lowry, A. R. (2017, November). USArray imaging of continental crust in the conterminous united states. *Tectonics*, *36*(12), 2882–2902. doi: 10.1002/2017TC004540

Ogden, C. S., Bastow, I. D., Gilligan, A., & Rondenay, S. (2019, August). A reappraisal of the H–κ stacking technique: implications for global crustal structure. *Geophysical Journal International*, *219*(3), 1491–1513. doi: 10.1093/gji/ggz364

Olugboji, T., Zhang, Z., Carr, S., Ekmekci, C., & Cetin, M. (2023, June). *On the detection of upper mantle discontinuities with radon-transformed PS receiver functions (CRISP-RF).* doi: 10.22541/essoar.168614559.90690115/v1

Olugboji, T. M., Park, J., Karato, S.-I., & Shinohara, M. (2016, April). Nature of the seismic lithosphere-asthenosphere boundary within normal oceanic mantle from high-resolution receiver functions: THE SEISMIC LAB IN NORMAL OCEANIC MANTLE. *Geochemistry, Geophysics, Geosystems*, *17*(4), 1265–1282. doi: 10.1002/2015GC006214

Park, J., & Levin, V. (2000, December). Receiver functions from multiple-taper spectral correlation estimates. *Bulletin of the Seismological Society of America*, *90*(6), 1507–1520. doi: 10.1785/0119990122

Park, J., & Levin, V. (2016, November). Anisotropic shear zones revealed by backazimuthal harmonics of teleseismic receiver functions. *Geophysical Journal International*, *207*(2), 1216–1243. doi: 10.1093/gji/ggw323

Parker, E. H., Jr, Hawman, R. B., Fischer, K. M., & Wagner, L. S. (2013, August). Crustal evolution across the southern appalachians: Initial results from the SESAME broadband array. *Geophysical research letters*, *40*(15), 3853–3857. doi: 10.1002/grl.50761

Philip Crotwell, H., & Owens, T. J. (2005, November). Automated receiver function processing. *Seismological Research Letters*, *76*(6), 702–709. doi: 10.1785/gssrl.76.6.702

Rivadeneyra-Vera, C., Bianchi, M., Assumpção, M., Cedraz, V., Julià, J., Rodríguez, M., … The "3-Basins" Project Team (2019, August). An updated crustal thickness map of central south america based on receiver function measurements in the region of the chaco, pantanal, and paraná basins, southwestern brazil. *Journal of Geophysical Research, [Solid Earth]*, *124*(8), 8491–8505. doi: 10.1029/2018jb016811

Rubio, G., Chen, Y., Sacchi, M. D., & Gu, Y. J. (2020, November). 3-D and 5-D reconstruction of P receiver functions via multichannel singular spectrum analysis. *Geophysical Journal International*, *225*(2), 1110–1128. doi: 10.1093/gji/ggaa541

Ryberg, T., & Weber, M. (2000, April). Receiver function arrays: a reflection seismic approach. *Geophysical Journal International*, *141*(1), 1–11. doi: 10.1046/j.1365-246X.2000.00077.x

Rychert, C. A., & Harmon, N. (2016). Stacked P-to-S and S-to-P receiver functions determination of crustal thickness, vp, and vs: The H-V stacking method. *Geophysical research letters*.

Rychert, C. A., Laske, G., Harmon, N., & Shearer, P. M. (2013, July). Seismic imaging of melt in a displaced hawaiian plume. *Nature geoscience*, *6*(8), 657–660. doi: 10.1038/ngeo1878

Shi, J., Wang, T., & Chen, L. (2020, August). Receiver function velocity analysis technique and its application to remove multiples. *Journal of Geophysical Research, [Solid Earth]*, *125*(8), B11309. doi: 10.1029/2020JB019420

Shi, Y., Gao, Y., Zhang, H., Zhang, Z., & Li, G. (2023, February). Crustal azimuthal anisotropy in the lateral collision zone of the SE margin of the tibetan plateau and its tectonic implications. *Geophysical Journal International*, *234*(1), 1–11. doi: 10.1093/gji/ggad059

Shibutani, T., Ueno, T., & Hirahara, K. (2008, April). Improvement in the Extended-Time multitaper receiver function estimation technique. *Bulletin of the Seismological Society of America*, *98*(2), 812–816. doi: 10.1785/0120070226

Stankiewicz, J., Chevrot, S., van der Hilst, R. D., & de Wit, M. J. (2002, April). Crustal thickness, discontinuity depth, and upper mantle structure beneath southern africa: constraints from body wave conversions. *Physics of the Earth and Planetary Interiors*, *130*(3), 235–251. doi: 10.1016/S0031-9201(02)00012-2

Tarkov, A. P., & Vavakin, V. V. (1982, July). Poisson's ratio behaviour in various crystalline rocks: application to the study of the earth's interior. *Physics of the Earth and Planetary Interiors*, *29*(1), 24–29. doi: 10.1016/0031-9201(82)90134-0

Thompson, D. A., Bastow, I. D., Helffrich, G., Kendall, J.-M., Wookey, J., Snyder, D. B., & Eaton, D. W. (2010, September). Precambrian crustal evolution: Seismic constraints from the canadian shield. *Earth and planetary science letters*, *297*(3), 655–666. doi: 10.1016/j.epsl.2010.07.021

Vanacore, E. A., Taymaz, T., & Saygin, E. (2013, January). Moho structure of the anatolian plate from receiver function analysis. *Geophysical Journal International*, *193*(1), 329–337. doi: 10.1093/gji/ggs107

Wang, F., Song, X., & Li, J. (2022, June). Deep learning-based$H$-κmethod (HkNet) for estimating crustal thickness andVP/vsratio from receiver functions. *Journal of Geophysical Research, [Solid Earth]*, *127*(6). doi: 10.1029/2022jb023944

Wang, K., Wu, S., & Tong, P. (2022). Crustal deformation in the sierra nevada and walker lane region inferred from P-Wave azimuthal anisotropy. *Journal of geophysical research*.

Wittlinger, G., Farra, V., Hetényi, G., Vergne, J., & Nábělek, J. (2009, June). Seismic velocities in southern tibet lower crust: a receiver function approach for eclogite detection. *Geophysical Journal International*, *177*(3), 1037–1049. doi: 10.1111/j.1365-246X.2008.04084.x

Xia, B., Thybo, H., & Artemieva, I. M. (2017, July). Seismic crustal structure of the north china craton and surrounding area: Synthesis and analysis. *Journal of Geophysical Research, [Solid Earth]*, *122*(7), 5181–5207. doi: 10.1002/2016jb013848

Yang, X., Pavlis, G. L., Hamburger, M. W., Marshak, S., Gilbert, H., Rupp, J., … Carpenter, N. S. (2017, August). Detailed crustal thickness variations beneath the illinois basin area: Implications for crustal evolution of the midcontinent. *Journal of Geophysical Research, [Solid Earth]*, *122*(8), 6323–6345. doi: 10.1002/2017jb014150

Yang, X., Pavlis, G. L., & Wang, Y. (2016, October). A quality control method for teleseismic P-Wave receiver functions. *Bulletin of the Seismological Society of America*, *106*(5), 1948–1962. doi: 10.1785/0120150347

Yeck, W. L., Sheehan, A. F., & Schulte-Pelkum, V. (2013). *Sequential H- stacking to obtain accurate crustal thicknesses beneath sedimentary basins* (Vol. 103) (No. 3). doi: 10.1785/0120120290

Yu, Y., Song, J., Liu, K. H., & Gao, S. S. (2015, May). Determining crustal structure beneath seismic stations overlying a low-velocity sedimentary layer using receiver functions. *Journal of Geophysical Research, [Solid Earth]*, *120*(5), 3208–3218. doi: 10.1002/2014JB011610

Yuan, H. (2015, August). Secular change in archaean crust formation recorded in western australia. *Nature geoscience*, *8*(10), 808–813. doi: 10.1038/ngeo2521

Zandt, G., & Ammon, C. J. (1995, March). Continental crust composition constrained by measurements of crustal poisson's ratio. *Nature*, *374*(6518), 152–154. doi: 10.1038/374152a0

Zhang, Q., Chen, Y., Zhang, F., & Chen, Y. (2022, March). Improving receiver function imaging with high-resolution radon transform. *Geophysical Journal International*, *230*(2), 1292–1304. doi: 10.1093/gji/ggac116

Zhang, Q., Wang, H., Chen, W., & Huang, G. (2021, January). A robust method for random noise suppression based on the radon transform. *Journal of Applied Geophysics*, *184*, 104183. doi: 10.1016/j.jappgeo.2020.104183

Zhang, Z., & Gao, Y. (2019, January). Crustal thicknesses and poisson's ratios beneath the Chuxiong-Simao basin in the southeast margin of the tibetan plateau. *Earth and Planetary Physics*, *3*(1), 69–84.

Zhang, Z., & Olugboji, T. (2021, May). The signature and elimination of sediment reverberations on submarine receiver functions. *Journal of Geophysical Research, [Solid Earth]*, *126*(5). doi: 10.1029/2020jb021567

Zhang, Z., & Olugboji, T. (2023, May). Lithospheric imaging through reverberant layers: Sediments, oceans, and glaciers. *Journal of Geophysical Research, [Solid Earth]*, *128*(5). doi: 10.1029/2022jb026348

Zhong, M., & Zhan, Z. (2020, July). An array-based receiver function deconvolution method: methodology and application. *Geophysical Journal International*, *222*(1), 1–14. doi: 10.1093/gji/ggaa113

Zhu, L., & Kanamori, H. (2000, February). Moho depth variation in southern california from teleseismic receiver functions. *Journal of geophysical research*, *105*(B2), 2969–2980. doi: 10.1029/1999JB900322